AIChE

Darcy's Law–Based Numerical Simulation for Modeling 3D Liquid Absorption into Porous Wicks

Reza Masoodi, Hua Tan, and Krishna M. Pillai
Laboratory for Flow and Transport Studies in Porous Media, Dept. of Mechanical Engineering, University of Wisconsin, Milwaukee, WI 53211

DOI 10.1002/aic.12343
Published online August 16, 2010 in Wiley Online Library (wileyonlinelibrary.com).

Liquid imbibition into polymer wicks, where a clear liquid front can be seen rising during the wicking process, is modeled using the concepts of flow in porous media. The flow of liquid behind the moving liquid front is modeled using the physics of single-phase flow in a porous medium where the Darcy's law is combined with the continuity equation and a capillary suction pressure is imposed at the liquid front. A novel numerical simulation PORE-FLOW© based on the finite element/control volume method is proposed to model such imbibitional flows in wicks of complex shapes. A validation of the simulation is obtained by achieving an excellent comparison of its predictions with an experimental result, an analytical solution, and the Washburn equation for the case of wicking against gravity in a cylindrical wick. The simulation is also used to predict a case of two-dimensional (2D) wicking in the altered cylindrical wicks with two different cross-sectional areas. Once again an excellent match is obtained with the experimental results, while analytical solutions for the single and double cross-section cases along with the Washburn equation fail to predict the 2D wicking. Later, some other types of altered wicks with sharp changes in their cross-sectional areas were analyzed numerically for their wicking behavior. It was observed that the height of liquid front in a vertical wick as a function of time, which is proportional to the history of liquid imbibed, is strongly dependent on the extent of reduction in the wick cross-sectional area as well as its location vis-à-vis the wick entrance. © 2010 American Institute of Chemical Engineers *AIChE J*, 57: 1132–1143, 2011
Keywords: absorption, wicking, imbibition, Washburn equation, Darcy's law, PORE-FLOW, FE/CV method, suction pressure, polymer wicks

Introduction

Wicking is suction of a liquid into a porous medium due to the negative capillary pressure at the liquid front. This suction capillary force arises as a result of wetting the surface of solid particles by the invading liquid that causes a change in the surface energy of the particles.

Correspondence concerning this article should be addressed to K. M. Pillai at krishna@uwm.edu.

Lucas,[1] Washburn,[2] and Poiseuille[3] were the three scientists who first studied the relation between wicking rate and time in a porous substrate. They modeled the imbibition of liquid in such a substrate as the Hagen–Poiseuille motion of liquid in a set of parallel capillary tubes behind a clear liquid front. They obtained a linear relation between the imbibed liquid mass and the square root of time when the effect of gravity is negligible. Szekely et al.[4] modified the Lucas–Washburn equation (also referred to as the Washburn equation) based on the capillary model to include the inertial forces and gravity effect and developed an ordinary

differential equation for the wicking rate. Masoodi et al.[5] showed a method to improve the predictions of liquid absorption in the polymer wicks using the capillary model: the hydraulic and capillary radii were shown to be independent and were to be measured separately to improve the predictions. In general, the Washburn equation has been studied extensively through experiments by several researchers, where the suggested equation was shown to be valid for most liquid-absorbing materials.[6] An excellent review of the most important previous work on wetting and wicking has been conducted by Kissa.[7] Some more recent reviews of literature on wicking phenomenon are available in Refs. 8,9.

Although the Washburn equation is an important relation that has been widely used for modeling absorption and wicking into porous substrates,[6] it is important to reflect on its limitations. One of its chief drawbacks is that as it is based on the model of Hagen–Poiseuille flow through a bundle of aligned and parallel capillary tubes, it can predict only one-dimensional (1D) imbibitional flows along the direction of capillary tubes. It cannot, due to the unidirectional nature of its flow model, predict the three-dimensional (3D) flows in wicks of complicated shapes. Moreover, the use of the Washburn equation implies that the complicated flow paths of liquids in a real porous medium are replaced by straight and hypothetical flow paths through cylindrical tubes. Hence, this model will always have a parameter, such as the hydraulic radius, which due to its origin in the pipe flow physics, is physically irrelevant and is often used as a fitting parameter.

While modeling the flow of water through sand, Darcy[10] proposed a simple relation between the average liquid velocity and the pressure drop that has stood the test of time as a reliable and simple model for the flow of single liquids (i.e., single-phase flows) in porous media. The flow physics based on the Darcy's law is quite well established in the porous media literature where it is regularly used to model flow in porous media.[10–12] Although relatively new in the field of wicking-flow modeling, the application of Darcy's law for modeling wicking flow in various types of porous media has been done in the recent past. Masoodi et al.[13] used Darcy's law–based models for predicting liquid absorption in the polymer wicks where a clear liquid front is discernible with only liquid flow behind the front, and the suction pressure* at the liquid front is the primary flow driver. Similarly, Pillai and Advani[14] had used a similar approach to model flow across a bank of parallel fibers.

Sometimes a clearly marked liquid front cannot be discerned in porous wicks during wicking and there is a gradual change (over a finite distance) in saturation from one to zero at the front.† For such situations, the unsaturated flow model has been used to model changes in saturation during the liquid imbibition process.[15–17] A heat equation–like equation called the Richard's equation has been used to model the time-dependent, diffusion-like migration of saturation during wicking. As the Richard's equation can be derived from the generalized Darcy's law used to model the simultaneous flow of two different fluids through a porous medium,[10] such an approach for modeling liquid imbibition in wicks can still be called a Darcy's law–based approach. Incidentally, the Richard's equation approach has been quite successful in modeling moisture distributions in soils above a water table.[10–12] However, the approach has its difficulties as complex experiments need to be used to measure important parameters such as the relative permeability and capillary pressure so that the moisture diffusion coefficient can be estimated. In the absence of an easy estimation of the coefficient, very often an exponential or power-law form of the moisture diffusion coefficient is assumed while applying this approach.[18]

In general, the use of the Darcy's law–based flow models not only raises the scientific level of a wicking flow model and enables one to draw on the vast research done in the area of porous-media flow and transport but also makes it possible to predict 3D wicking flows in porous wicks of complex shapes. In this article, we are going to model 3D liquid flow in polymer wicks of complex shapes using the Darcy's law–based approach using the single-phase flow assumption behind a clearly defined liquid front. PORE-FLOW©, a computer program based on the finite element/control volume (FE/CV) method to model free-surface flows in porous media,[19] is used to solve the flow equations within the complex-shaped polymer wicks and to predict the location of liquid front (It is the first time that such an FE/CV-based flow-modeling software is used to solve for such 3D wicking flows). Complex (altered) wicks are created from the ordinary cylindrical polymer wicks by changing their diameters for certain lengths at certain axial locations. First, the experimental validation of our computational flow model will be undertaken for the simple and altered wicks. Then, this numerical study will estimate how effective this technique (of altering the cross-sectional areas) is in controlling and reducing the liquid absorption rate in wicks.

Geometry of Plain and Altered Wicks

As we can see in Figure 1a, commercial polymer wicks are cylindrical in shape and have a constant diameter along their entire length. A typical diameter and length of such wicks are 0.0072 and 0.075 m, respectively. We created an altered wick by sharply changing the wick diameter along the wick length at several locations with the help of a milling machine. Figure 1b shows planned changes in the plain wick and the names assigned to the dimensions to be changed. Table 1 lists the values of these dimensions in the five different altered wicks considered in this study. In the table, wick A is a simple wick without any manipulation while wicks B, C, D, and E are altered wicks.

Theory of Wicking

During a previously reported study,[13] we tested 10 different polymer wicks and discovered that six of them created a clear liquid front during the wicking process; in the other four wicks, a capillary fingering effect caused the liquid front to be unstable and no clear front could be discerned. In other words, the saturation changed from one to zero over a finite distance, unlike the case of a clear liquid front where it jumps from one to zero over a very small distance. It means that we can use the single-phase Darcy's law models

*Using the energy balance principle, a new formula to predict the suction pressure in the porous media composed of sphere-like polymer beads was proposed.[13]
†Saturation is defined as the fraction of pore volume of the porous medium occupied by the invading liquid. As a result, the saturation takes a value between zero and unity.

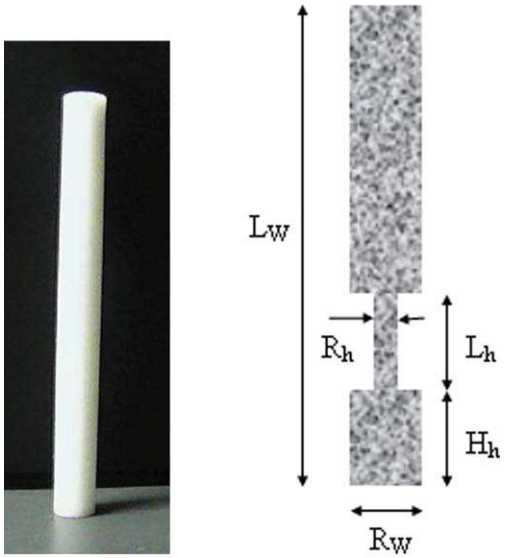

Figure 1. (a) A photo of a cylindrical polymer wick; (b) an altered wick section showing changes in its cross-sectional area as well as various associated dimensions.

to study fluid flow in about 60% of the wicks, while its two-phase version will be needed for modeling the remaining 40%. The wicks that we have considered in this study belong to the first group. Therefore, the theoretical approach presented here involves the single-phase flow inside porous wicks with a clear liquid front.

The momentum equation, also called the Darcy's law, for the flow of a single liquid in an isotropic porous medium under isothermal conditions is

$$\tilde{V} = -\frac{K}{\mu}\tilde{\nabla} P \tag{1}$$

where $\tilde{V}$ is volume-averaged liquid velocity and P is the pore-averaged modified pressure.[‡] Here, K is the permeability of the porous medium while μ is the liquid viscosity. Another governing equation for the flow of an incompressible liquid in a solid porous medium is the macroscopic continuity or mass balance equation

$$\tilde{\nabla} \cdot \tilde{V} = 0 \tag{2}$$

The effect of gravity-induced liquid motion in a porous medium and pore averaged hydrodynamic pressure p are included in the modified pressure P as

$$P = p + \rho g h \tag{3}$$

where h is the height of a point within the fully saturated porous medium. If the permeability and viscosity are considered to be constant, then a combination of Eq. 1 with Eq. 2 leads to a Laplace equation for the modified pressure as

$$\nabla^2 P = 0 \tag{4}$$

After solving Eq. 4 for P in a domain, Eq. 1 yields the velocity distribution and subsequently, the location of liquid front in the wick.

Analytical Solution for the Single Cross-Section Wick

For now, we are going to consider the 1D fluid motion in a simple wick as shown in Figure 1a with a constant cross-sectional area. Figure 2a shows the test setup consisting of the dynamic contact angle analyzer, which is usually used for the wicking tests. The analytical solution for the liquid motion will be presented in brief here—details of its derivation can be found elsewhere.[13]

For the 1D flow described in Figure 2b, the Laplace equation for the modified pressure, Eq. 4, reduces to

$$\frac{d^2 P}{dh^2} = 0 \tag{5}$$

The relevant boundary conditions in terms of the pore averaged hydrodynamic pressure p are

$$p = p_{\text{atm}} \quad \text{at} \quad h = 0 \tag{6a}$$

$$p = p_{\text{atm}} - p_{\text{s}} \quad \text{at} \quad h = h_{\text{f}} \tag{6b}$$

The suction pressure p_{s}, created at the liquid front due to the capillary action, is responsible for "pulling up" the liquid column along the vertical wick. Using Eq. 3, Eqs. 6a,b can be transformed in terms of the modified pressure P as

$$P = p_{\text{atm}} \quad \text{at} \quad h = 0 \tag{7a}$$

$$P = (p_{\text{atm}} - p_{\text{s}}) + \rho g h_{\text{f}} \quad \text{at} \quad h = h_{\text{f}} \tag{7b}$$

The general solution of Eq. 5 using boundary conditions 7a and 7b results into the following expression for the modified pressure

$$P(h) = p_{\text{atm}} + \rho g h - p_{\text{s}} \frac{h}{h_{\text{f}}} \tag{8}$$

Note that this solution is valid for $0 \le h \le h_{\text{f}}\,(t)$. The liquid-front location h_{f} can be obtained by relating the front speed $\frac{dh_{\text{f}}}{dt}$ with the Darcy velocity (obtained from Eq. 1) at the front as

$$\frac{dh_{\text{f}}}{dt} = \frac{V(h = h_{\text{f}})}{\varepsilon} = -\frac{K}{\varepsilon \mu}\frac{dP}{dh} \tag{9}$$

Table 1. Values of the Dimensions Shown in Figure 1b for All the Five Wicks Studied in This Article

Wick	L_{w} (mm)	R_{w} (mm)	R_{h} (mm)	L_{h} (mm)	H_{h} (mm)
A	75	7	0	0	0
B	75	7	3	5	10
C	75	7	5	5	10
D	75	7	3	15	0
E	75	7	5	15	0

Figure 8 provides an easy visualization of the geometries B, C, D, and E.

[‡]The macroscopic flow description in porous media seeks to average flow quantities over the pore space of an averaging volume and thus create a continuum of such volume-averaged quantities for the purposes of flow modeling. The volume average, also referred to as the phase average, and the pore averaged, also referred to as the intrinsic phase average, are two different types of averages used in porous media studies.[20] The former pertains to averaging a quantity over the whole of the averaging volume, while the latter refers to averaging over the pore space within the averaging volume.

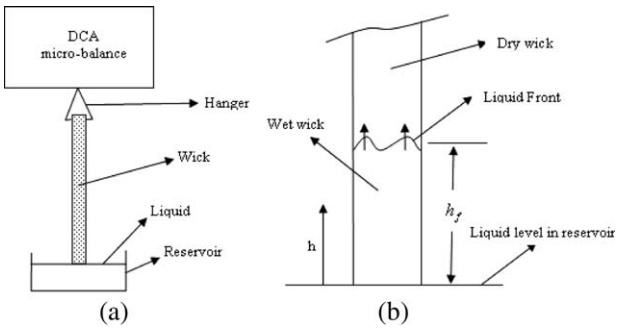

Figure 2. (a) A schematic of the experimental wicking test setup; (b) a schematic of the 1D flow and liquid-front position in a plain cylindrical wick.[5]

Using Eq. 8 in Eq. 9 leads to

$$\frac{dh_f}{dt} = \frac{K}{\varepsilon\mu}\left(\frac{p_s}{h_f} - \rho g\right) \tag{10}$$

which is an ordinary differential equation to be solved with the initial condition h_f $(t = 0) = 0$. After the separation of variables and subsequent integration, the final implicit equation for the liquid-front height h_f in the wick as a function of time is

$$p_s \ln\left|\frac{p_s}{p_s - \rho g h_f}\right| - \rho g h_f = \frac{\rho^2 g^2 K}{\varepsilon\mu} t \tag{11}$$

Once the location of liquid front h_f is known, following equation can be used to estimate the absorbed liquid mass as a function of time

$$m = \varepsilon\rho\pi R_w^2 h_f \tag{12}$$

Using the energy balance model suggested earlier for polymer wicks,[13] one can estimate p_s as

$$p_s = \frac{3(1-\varepsilon)\gamma\cos(\theta)}{\varepsilon R_e} \tag{13}$$

where R_e, the effective beads radius, can be computed using the equation

$$R_e = \frac{\int_0^\infty R_b^3 \phi(R_b) dR_b}{\int_0^\infty R_b^2 \phi(R_b) dR_b} \tag{14}$$

with ϕ (R_b) being the probability density function for bead radius[§] R_b.

Analytical Solution for an Altered Wick with a Step Change in Cross-Sectional Area

It turns out that the flow physics applied for developing an analytical solution for a plain cylindrical wick in the last section can also be used to fashion an analytical solution for wicking in an altered wick with step-like variations in its cross-sectional area.

For a wick with a sharp change in the cross-sectional area, such as the wick "D" of Table 1, we have two regions: Region 1 with a smaller wick radius R_{w1} up to height h_i, and Region 2 with larger wick radius R_{w2} (see Figure 3).

[§]The polymer wicks are made from polymer beads through a sintering process. So on studying the wick cross section under a microscope, one cannot only estimate bead radii but also study their distribution.[13]

Fluid flow is expected to be 1D everywhere in the altered wicks except near the point of change in the wick cross-sectional area. If we assume the flow to be 1D in the entire wick, then there will be an error in our analytical solution due to the anticipated three-dimensional (3D) flow around the sharp change in the cross-sectional area. However, this error is expected to decrease as the front moves away from this point. If the difference between R_{w1} and R_{w2} is small, then this error is expected to be insignificant as well.

On imposing the 1D flow assumption in each region of Figure 3, the Laplace equation for pressure, Eq. 4, reduces to

$$\frac{d^2P}{dh^2} = 0 \tag{15}$$

Solution of this equation in Regions 1 and 2 can be expressed as

$$P_1 = B_1 h + C_1 \tag{16a}$$

$$P_2 = B_2 h + C_2 \tag{16b}$$

where subscripts 1 and 2 refer to the two wick regions. Now the four boundary conditions needed to find four constants in Eqs. 16a,b are

$$P_1 = p_{atm} \text{ at } h = 0 \tag{17a}$$

$$P_1 = P_2 \text{ at } h = h_i \tag{17b}$$

$$P_2 = p_{atm} - p_s + \rho g h_f \text{ at } h = h_f \tag{17c}$$

$$Q_1 = Q_2 \Rightarrow B_1 R_{w1}^2 = B_2 R_{w2}^2 \text{ at } h = h_i \tag{17d}$$

The last condition is obtained from the equality of mass flux at the common boundary of Regions 1 and 2. The use of these four boundary conditions in Eqs. (16) yields the following expressions for the four constants.

$$B_1 = \frac{R_{w2}^2}{R_{w1}^2} \frac{\rho g h_f - p_s}{h_f - h_i + h_i \frac{R_{w2}^2}{R_{w1}^2}} \tag{18a}$$

$$C_1 = p_{atm} \tag{18b}$$

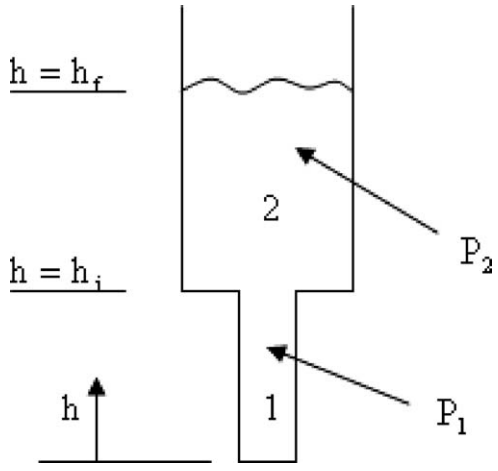

Figure 3. Different regions and liquid-front location in an altered wick with two different cross-sectional areas.

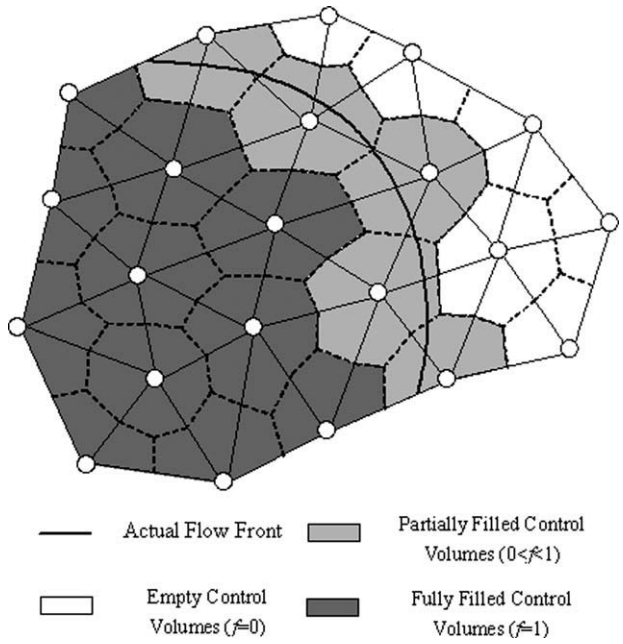

Figure 4. A schematic describing a typical finite element mesh along with the surrounding control volumes for application with the FE/CV method to model the motion of liquid front in the wicks.

$$B_2 = \frac{\rho g h_f - p_s}{h_f - h_i + h_i \frac{R_{w2}^2}{R_{w1}^2}} \tag{18c}$$

$$C_2 = p_{atm} - p_s + \rho g h_f - h_f \frac{\rho g h_f - p_s}{h_f - h_i + h_i \frac{R_{w2}^2}{R_{w1}^2}} \tag{18d}$$

On using Darcy's law in association with the front velocity in Region 2, we get

$$\frac{dh_f}{dt} = -\frac{K}{\varepsilon\mu}\frac{dP_2}{dh}\bigg|_{h=h_f} = -\frac{K}{\varepsilon\mu}\frac{\rho g h_f - p_s}{h_f - h_i + h_i \frac{R_{w2}^2}{R_{w1}^2}} \tag{19}$$

On integrating after separating the variables and later assuming $h_f(t_i) = h_i$, we can derive following expression for Region 2.

$$t = t_i + \frac{\varepsilon\mu}{K\rho g}\left[h_i - h_f + \frac{p_s - \rho g h_i\left(1 - \frac{R_{w2}^2}{R_{w1}^2}\right)}{\rho g}\ln\frac{p_s - \rho g h_i}{p_s - \rho g h_f}\right] \tag{20}$$

Note that we can get the equivalent relation for Region 1 by imposing the condition $h_i = t_i = 0$ in Eq. 20 and obtain an expression identical to Eq. 11. We can develop the following compact form for the implicit expressions for $h_f(t)$ in both the wick regions.

$$t = \begin{cases} t_i + \frac{\varepsilon\mu}{K\rho g}\left[h_i - h_f + \frac{p_s - \rho g h_i\left(1 - \frac{R_{w2}^2}{R_{w1}^2}\right)}{\rho g}\ln\frac{p_s - \rho g h_i}{p_s - \rho g h_f}\right] & , \; h_f > h_i \\ -\frac{\varepsilon\mu h_f}{K\rho g} + \frac{\varepsilon\mu p_s}{K\rho^2 g^2}\ln\frac{p_s}{p_s - \rho g h_f} & , \; h_f < h_i \end{cases} \tag{21}$$

Although we can develop a similar analytical solution for the other wick type (wicks B and C of Table 1), we will confine the development of such an analytical solution to the present case only. This is because we have used a wick of the type shown in Figure 3 for conducting experiments and used those results for validating our simulation. Hence, the analytical solution will be useful in providing another point of reference for our code.

Analytical Solution for a Simple Wick Using the Modified Washburn's Capillary Model

As mentioned in the Introduction, the wicking model proposed by Washburn remains a powerful technique used by the research community to predict 1D wicking in porous substrates. We intend to use it as the third analytical solution to highlight its limitation for the cases where 3D flows are involved during wicking.

Under the Washburn's capillary model, the considered porous medium, a polymer wick, will be assumed to be equivalent to a bundle of vertically aligned capillary tubes. If the gravity effect is negligible, then the capillary model yields the well-

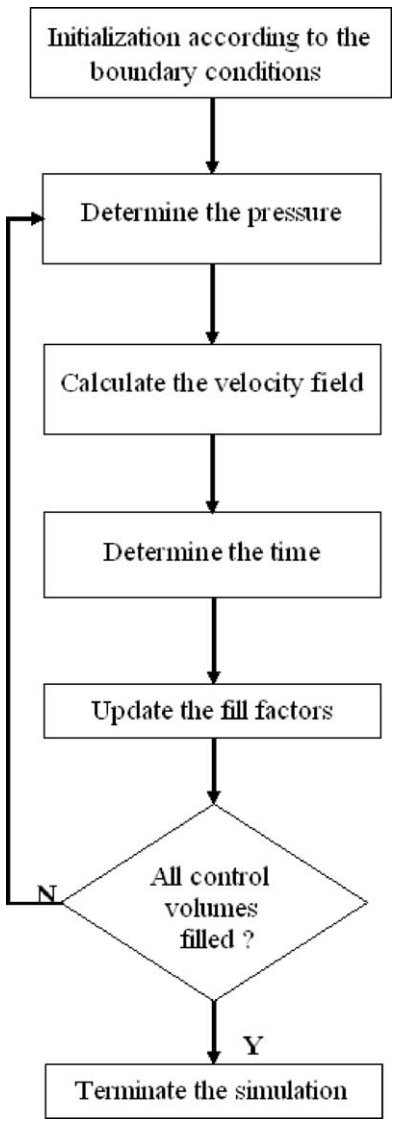

Figure 5. A flow chart describing the FE/CV algorithm.

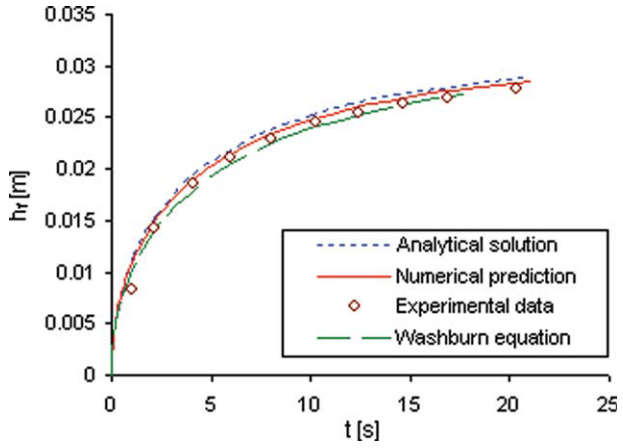

Figure 6. A comparison of the numerical prediction with the experimental result and analytical solution for the case of wicking in a simple wick.

known form of Washburn equation that predicts the location of liquid front h_f as a function of time t as

$$h_f = \sqrt{\frac{\gamma D_e \cos(\theta)}{4\mu} t} \tag{22}$$

where D_e, the effective pore diameter, is obtained through

$$D_e = \frac{D_h^2}{D_c} \tag{23}$$

such that D_c is the capillary diameter and D_h is the hydraulic diameter of the capillary tubes (The capillary and hydraulic radii, R_c and R_h, respectively, are half of these diameters).

In general cases where the gravity is not negligible, one can derive an implicit relation between h_f and time t as

$$p_c \ln\left|\frac{p_c}{p_c - \rho g h_f}\right| - \rho g h_f = \frac{\rho^2 g^2 R_h^2}{8\mu} t \tag{24}$$

which can be termed as the alternate form of the Washburn equation with the gravity effects. The capillary (suction) pressure for capillary tubes p_c, a parameter in Eq. 24, is obtained with the help of the Laplace equation as

$$p_c = \frac{2\gamma \cos(\theta)}{R_c} \tag{25}$$

As the right-hand side of Eq. 24, a linear expression in t, is a function of the left-hand side expression for h_f, it is very easy to estimate t for a given value of h_f—the ordered pairs for Washburn equation plots of Figures 6 and 7a were made using this method.

A detailed derivation of the forms of Washburn equation can be found in Ref. 5

Numerical Approach

We will describe an FE/CV method to solve the 3D wicking flow, using the single-phase flow physics described in geometry of plain and altered wicks sections by Eqs. 1–4. The FE/CV is a well-proven method to model free-surface flows in porous media. One of the chief applications of the method is in numerically simulating the transient mold filling in the liquid composite molding processes used for the manufacture of composite materials.[21] The FE/CV method will be used here to model the transient free-surface problem encountered during wicking in porous wicks.

FE/CV Method

In the proposed algorithm, the transient fluid flow in the wicks involving a moving boundary is divided into multiple time steps. After assuming a quasi-steady condition during each time step, Eq. 4 is first solved for modified pressure in the wick region that has been saturated by the moving liquid front. We then use the computed pressure field to estimate the velocity field using Eqs. 1 and 2, and then use the field to find the new location of liquid front at each time step.

As the liquid front is moving, so the hybrid FE/CV method is used to track the flow surface. This method uses an Eulerian fixed mesh to track the flow front and is highly efficient computationally as it avoids frequent remeshing of the flow domain as opposed to a Lagrangian algorithm. Equation 4 is first solved in the fully saturated region behind the moving front. As shown in Figure 4, P behind the moving wicking front is solved in the fixed FE mesh. By applying the standard Galerkin weighted residual method to Eq. 4 and integrating by parts, the weak formulation of pressure governing equation is given by

$$\int_\Omega \frac{K}{\mu}\left(\frac{\partial w}{\partial x}\frac{\partial p}{\partial x} + \frac{\partial w}{\partial y}\frac{\partial p}{\partial y}\right) dxdy = \oint_\Gamma w(\mathrm{v.n}) ds \tag{26}$$

where w is the weight function, $\boldsymbol{v}$ is the Darcy velocity, and $\boldsymbol{n}$ is the unit vector normal to the boundary.[22] The pressure is approximated by the shape function N and nodal pressure p as

$$p = \sum_{j=1}^{n} N_j(x,y) p_j \tag{27}$$

where n is the number of nodes in an element. On substituting Eq. 27 into the weak formulation Eq. 26 while using the relation $w_i = N_i$, we obtain a set of linear equations for one FE as

$$\left[\sum_{j=1}^{n} \int_{\Omega^e} \frac{K}{\mu}\left(\frac{\partial N_i}{\partial x}\frac{\partial N_j}{\partial x} + \frac{\partial N_i}{\partial y}\frac{\partial N_j}{\partial y}\right) dxdy\right] p_j = \oint_{\Gamma^e} N_i(\mathrm{v.n}) ds \tag{28}$$

As the domain is divided into a number of elements, the assembly of Eq. 28 for each element results in a set of algebraic linear equations as

$$[\mathbf{A}]\{\mathbf{P}\} = \{\mathbf{F}\} \tag{29}$$

where the coefficient matrices are defined as

$$K_{ij}^e = \sum_{j=1}^{n} \int_{\Omega^e} \frac{K}{\mu}\left(\frac{\partial N_i}{\partial x}\frac{\partial N_j}{\partial x} + \frac{\partial N_i}{\partial y}\frac{\partial N_j}{\partial y}\right) dxdy$$

$$f_i^e = \oint_{\Gamma^e} N_i(\mathrm{v.n}) ds \quad \mathbf{A} = \sum_{e=1}^{ne} K_{ij}^e \qquad \mathbf{F} = \sum_{e=1}^{ne} f_j^e \tag{30}$$

The velocity normal to the boundary is zero except at the inlet, where a nonzero value is automatically satisfied by the FE method (often referred to as the natural boundary condition). The capillary

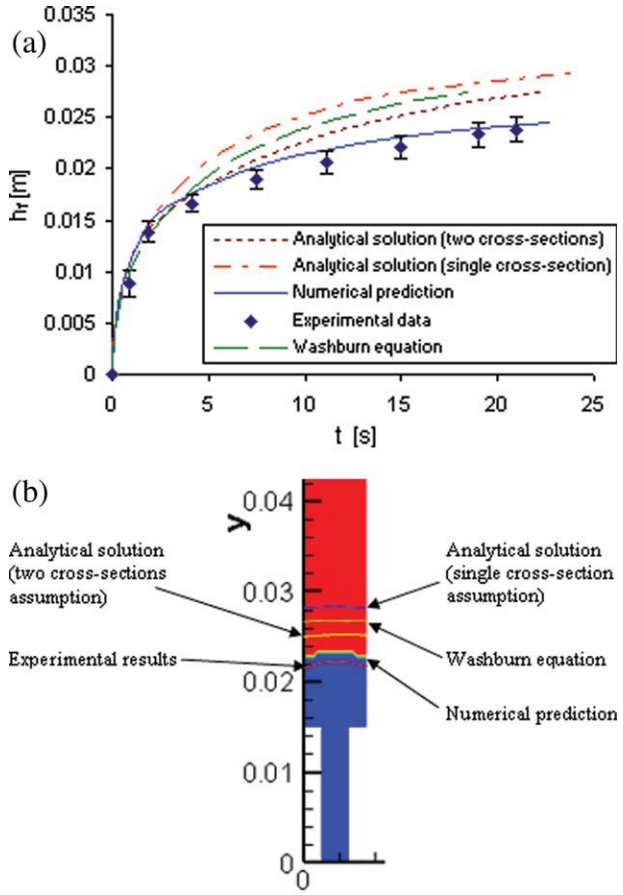

Figure 7. For wicking in wick "D," a comparison of the numerical prediction with the analytical solutions corresponding to the one and two different cross sections for wick and the experimental result.

(a) A comparison of the flow-front height h_f vs. time t plots. Scatter bars show confidence interval of 95%. (b) A comparison of the flow-front locations for the wick "D" at time t = 20 s. [Color figure can be viewed in the online issue, which is available at wileyonlinelibrary.com.]

suction pressure p_s, obtained from Eq. 13, will be used for imposing the modified pressure boundary condition at the front using Eq. 7b. The pressure boundary conditions implemented in our model are

$$P = p_{atm} \quad \text{at} \quad h = 0 \tag{31a}$$

$$\frac{dP}{dn} = 0 \quad \text{at} \quad R = R_w \quad \text{for } h < h_f \tag{31b}$$

$$P = (p_{atm} - p_s) + \rho g h_f \quad \text{at} \quad h = h_f \tag{31c}$$

Note that the hydrostatic variation in liquid pressure is accounted for in the modified pressure through the use of expression given in Eq. 3.

The final set of linear algebraic equations corresponding to Eq. 29 are solved by a large parallel sparse direct solver MUMPS.[23] Later, the distribution of P behind the front is used to furnish V with the help of Darcy's law, Eq. 1, at the interfaces of the CSs defined around the node points, which is then used to determine the flow-front velocity and to advance the front after each time step as follows.

We have defined a filling factor f_i that is used to track saturation in the CV defined around any element i and can be expressed as

$f_i = 1$ for CVs behind the liquid front that are filled with the liquid (32a)

$0 \le f_i \le 1$ for CVs near the liquid front that filled partially with the liquid (32b)

$f_i = 0$ for CVs beyond the liquid front in the dry region (32c)

The time increment of each time step for advancing the flow front is determined by the shortest time to completely fill one CV expressed as

$$\Delta t = \min\left[\frac{(1 - f_i)\varepsilon V_i}{Q_i}\right] \tag{33}$$

where Q_i is the flow rate into a CV computed by integrating normal velocity on the surface of the CV as

$$Q_i = \int_{\Gamma_{cv}} -(\vec{V}.\hat{n})d\Gamma_{cv} = \sum_k \int_{\Gamma_k} -(\vec{V}.\hat{n})d\Gamma_k \tag{34}$$

After each time step t_n, we have to update the filling factor before going into next time step $t_n + 1$; the following expression is used to modify the filling factor for each time increment

$$f_i^{t_{n+1}} = f_i^{t_n} + \frac{Q_i}{\varepsilon V_i}\Delta t \tag{35}$$

This FE/CV algorithm (described using a flow chart in Figure 5) is used by PORE-FLOW©, a computer program developed at University of Wisconsin, Milwaukee[19] for modeling liquid flow in porous media. Note that the FE/CV algorithm has been used in the past to model wetting of fibrous porous media in liquid molding processes to manufacture polymer composites[21,22,24]; however, this is the first time that this simulation technique is used to model the wicking flows in polymer wicks.

Note that as the flow is essentially 1D along the wick length, except near places with sharp jumps in the cross-sectional area, a 2D flow simulation is enough to capture fluid flow in the axisymmetric geometry of the essential cylindrical wicks. So, even though a full 3D flow simulation can be conducted by PORE-FLOW for more complex wick geometries, a 2D flow simulation is sufficient in the modeling of wicking flow in this article. As a result, the meshes described in Figure 8 are flat, 2D shell meshes. However, a thickness is assigned to these meshes to conduct flow rate computations while doing mass flow estimation into the CVs. The thickness is chosen in such a way that the cross-sectional area of the entrance of 2D meshes matches the wick cross-sectional area—such a step ensures that the Darcy velocities in the real wick and the 2D FE model are equal for a given flow rate.

Results and Discussions

It is important to test the accuracy of our simulation. Therefore, we tested our code against experimental results as well as the analytical solutions.

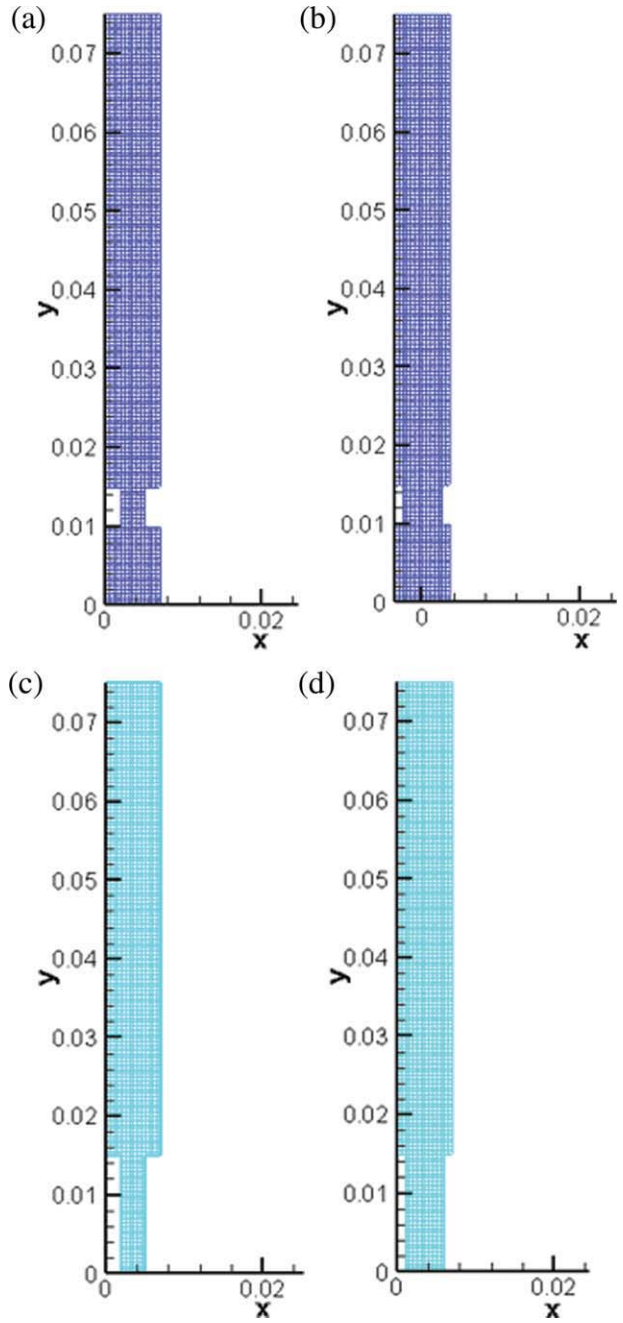

Figure 8. The finite element meshes generated for the wicks B, C, D, and E.

(a) Wick B. (b) Wick C. (c) Wick D. (d) Wick E. [Color figure can be viewed in the online issue, which is available at wileyonlinelibrary.com.]

The wicking experiments were conducted using a microbalance shown in Figure 2. The cylindrical wick (simple or adapted) was suspended from the balance and made to touch the surface of a liquid; the wicking starts as soon as the contact was made. The weight gain in the wick due to liquid imbibition is recorded by the microbalance and is recorded with the help of a computerized data acquisition system hooked to the microbalance (Details of the wicking experiment are given elsewhere in Ref. 13). The properties of the wick and liquid used in our experiments are listed in Table 2.

First, the case of 1D wicking in a simple wick, as analyzed earlier, will be considered. The analytical solutions for this case are given by the Darcy's law approach (Eq. 11) and the Washburn equation (Eq. 24). A plot of the front height predicted as a function of time is given in Figure 6—as we can see, the numerical prediction match very well with the analytical solutions, which in turn match very well with the experimental results. So it is heartening to see such a good validation of our numerical simulation.

Now we consider a more difficult case of wicking in a cylindrical wick with a single step change in the diameter, i.e., wicking in wick D, for the validation of our code. Figure 7 shows a comparison of the numerical prediction of the flow-front height h_f as a function of time t with the analytical 1D solutions developed for one and two different cross sections of the wick (Eqs. 11 and 21, respectively), the Washburn equation (Eq. 24), and the experimental data for wick "D." In the plot of experimental results, the confidence interval of 95% is shown by the scatter bars. Figure 7 shows that the use of the double cross-section model when compared with the single cross-section model improves the analytical prediction but it is still not as good as the numerical prediction. Similarly, the limitations of the 1D approximation–based Washburn equation are exposed in this case of the 3D wicking flows where the equation over predict the flow-front height.

Such a good validation for the cases of wicking in the simple 1D flow and the altered 3D flow wicks inspires confidence in the accuracy and correctness of our simulation PORE-FLOW©.

Let us turn our attention to a parametric study done with the four different geometries of the altered wick listed in Table 1 and their FEM meshes shown in Figure 8. Numerical simulations for wicking were done for these four different altered wicks with four different sharp changes in their cross-sectional areas. The results are compared with each other as well as with the predictions for the simple wick with a constant cross-sectional area.

Figures 9 and 10 show the liquid-front movements in the wicks C and D as predicted by PORE-FLOW©. Figure 9 shows that after entering the notched area, the liquid front near the boundaries is a little higher than the liquid front in the middle. The reason for this discrepancy is that the flow

Table 2. Characteristics of the Wicks and the Liquid Used in Our Validation Experiments*

Property	Value	Unit
Density of the liquid	773	Kg/m^3
Viscosity of the liquid	0.00334	m Pa s
Surface tension of liquid†	22.24	mJ/m^2
Length of wick L_w	0.076	m
Wick radius R_w	0.0036	m
Wick porosity ε	0.4	–
Effective bead radius R_e	482	μm
Permeability K	4.84e − 10	m^2
Contact angle θ	0	–

The wick was made from polypropylene while the liquid was hexadecane.
*The experimental procedures for measuring these parameters are explained in Ref. 13.
†Previously, we had used a higher value for surface tension in Ref. 13, which came from some other source (Ref. 29); while here, we have measured the value of surface tension directly.

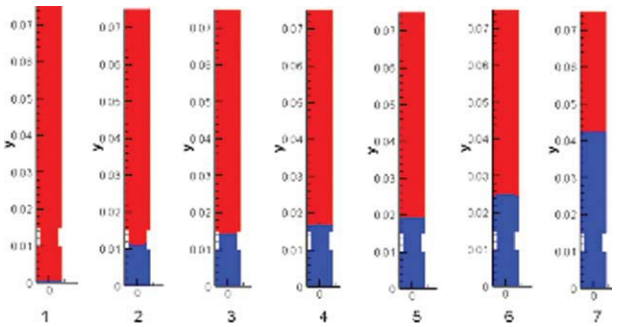

Figure 9. Pattern of liquid-front movement in the wick C.

[Color figure can be viewed in the online issue, which is available at wileyonlinelibrary.com.]

that is to go in the "removed" pores must be distributed into all the remains pores; however, as the pores close to the boundaries are closest to the removed pores, so they have a higher flow rate compared with the pores in the middle that are far away from the removed pores. Note that this imbalance is corrected after a while as the flow front becomes perfectly horizontal once again. We see an exactly opposite effect after the passage of the front through a constriction and into a wider cross section. In the parts 4 and 6 of Figure 9 as well as in parts 2 to 5 of Figure 10, we can observe a little bulging of the front due to an enlargement in the cross-sectional area. It implies that the pores in the middle regions face higher flow rates when compared with the pores in the border regions, and hence, the liquid front is a little higher in the middle after the expansion of the wick cross-sectional area. This unbalance in the flow rate is compensated as the front moves away from the expansion point, and the liquid front acquires the perfectly horizontal profile during the later stages of the wicking process.

Figure 11a plots the evolution of the dimensionless liquid-front height (h_f/L_w) for the wicks A, C, and E. Note that the slope of these plots is equal to the speed of the liquid front. It is clear that beyond $t = 1$ s, the liquid front has traveled the farthest in the simple wick A. However, the speeds of their liquid fronts are almost identical beyond $t = 5$ s; hence, the curves are almost parallel beyond this point. It is clear that reduction in the distance traveled as well as reduction in the speed is related to (1) the reduction in the cross-sectional area of these wicks and (2) the length over which the reduced area is maintained. Although the diameter reduces

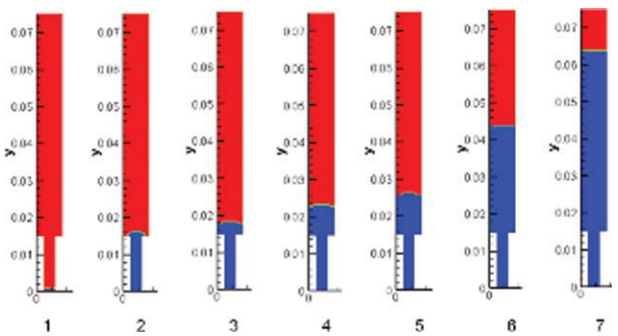

Figure 10. Pattern of liquid-front movement in the wick D.

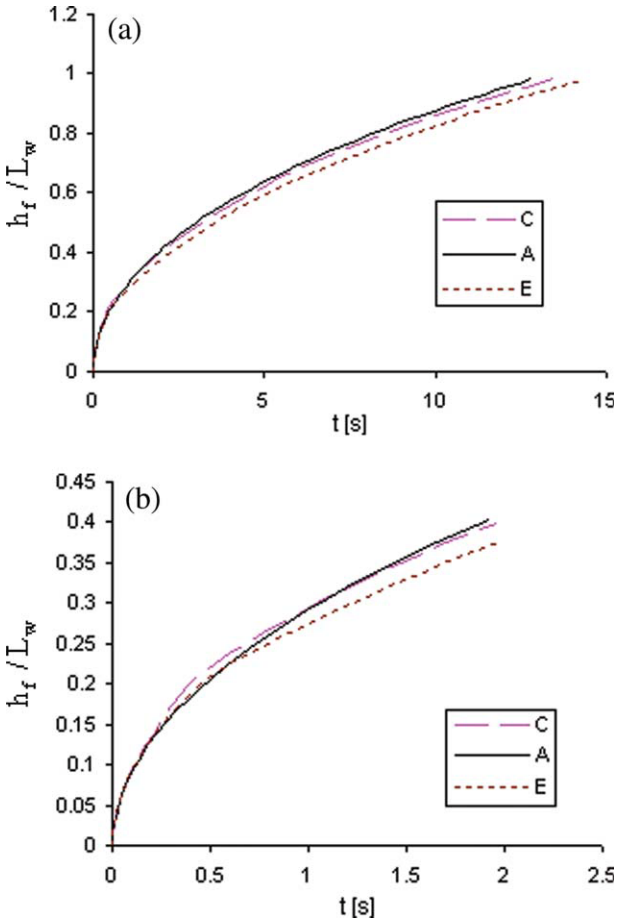

Figure 11. A comparison of evolution of the dimensionless and numerically predicted liquid-front height (h_f/L_w) in the wicks A, C, and E.

(a) The comparison till the time of full saturation. (b) The comparison in the first 2 s. [Color figure can be viewed in the online issue, which is available at wileyonlinelibrary.com.]

by same amount in the wicks C and E, the smaller diameter is retained for a longer length in E. If we propose that these two factors are related to the resistance offered by a wick, then the resistance in the wick C is less than that in the wick E. As a result, the liquid front travels farther in the wick C when compared with the wick E. Figure 11b gives more details of the first 2 s of the absorption process. Initially, the wicking speeds in A, C, and E are almost identical. This is understandable as the wicking process is purely 1D in all these wicks in the beginning and hence, variations in the cross-sectional areas are immaterial. However, the wicking speeds up in C at around $t = 0.25$ s when the front hits the first notch of the constriction in C. The C and E fronts are in the constricted region till $t = 0.5$ s; from this point onward, the sectional area remains constant in these two wicks and hence, we see a constant pattern for the C and E curves. Note that at $t = 0.45$ s, the liquid-front height is about 9% higher in C compared with A.

Figure 12 plots the dimensionless liquid-front positions as a function of time for the wicks A, B, and D. As the wicks B

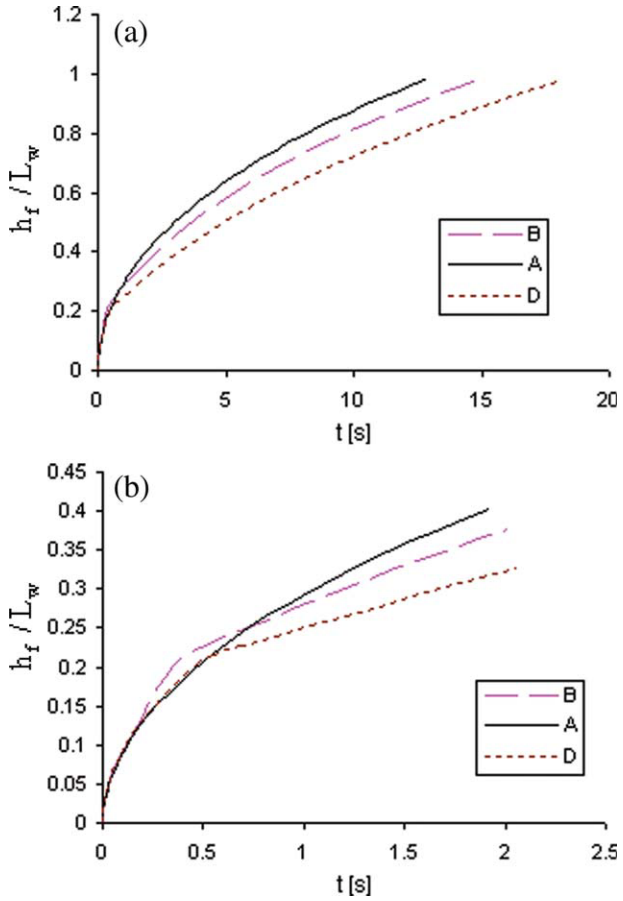

Figure 12. A comparison of evolution of the dimensionless and numerically predicted liquid-front height (h_f/L_w) in the wicks A, B, and D.

(a) The comparison till the time of full saturation. (b) The comparison in the first 2 s. [Color figure can be viewed in the online issue, which is available at wileyonlinelibrary.com.]

and D are similar in shape to the wicks C and E, respectively, we see the same patterns as in Figure 11. However, the differences in terms of diameters between the altered wicks B and D with the simple wick A are more. Once again, in comparison to the simple wick A, the absorption speed has reduced in B and D due to a reduction in the cross-sectional area. As before, the reduction in diameter is the same in wicks B and D but the length of the constriction is longer in D. According to Figure 12a, the curve of D is below the curve B, which implies that the wick D offers more resistance to wicking when compared with B. Figure 12b gives more detail of the first 2 s of absorption. The front is in the notched region till $t = 0.45$ s; from $t = 0.45$ s onward, the sectional area remains constant for altered wicks and hence, we see a constant, almost linear pattern for each curve. Based on Figure 12b, the absorption rate in the wick D is similar to that of the wick A for up to $t = 0.5$ s and after that it decreases. The wick B has a higher liquid front than the wick A from $t = 0.2$ s to $t = 0.75$ s. The liquid-front height in B is about 18% higher than in A at $t = 0.39$ s, but then B's front speed decreases and its front height becomes 6% less than that of A after 12 s.

Figure 13 compares the dimensionless liquid-front heights as a function of time in all the four altered wicks. The wicks B and C have the same shape but B has a smaller diameter in the constricted region. Similarly, the wicks D and E also have the same shape but the diameter of the constricted region is smaller in D than in E. According to Figure 13a, the highest wicking rate is in wick C, while the lowest is in wick D. The time to traverse the whole length of the wick (0.075 m) is surprisingly almost identical in the wicks B and E, even though they are completely different in terms of their shapes. According to Figure 13b, just after leaving the sharp changes in the cross-sectional area (i.e., around $t = 0.4$ s), the highest liquid front is in the wick B while the lowest liquid front is in the wick E.

We would like to evaluate the relative performance of the altered wicks with respect to the simple wick in yet another way; the middle column of Table 3 lists the exact time needed for liquid front to reach the height of 0.07 m (Since the length of a commercial wick is between 0.07 and 0.075 m; therefore, we chose this final height for the comparison of wicking performance of different wicks). As shown in the

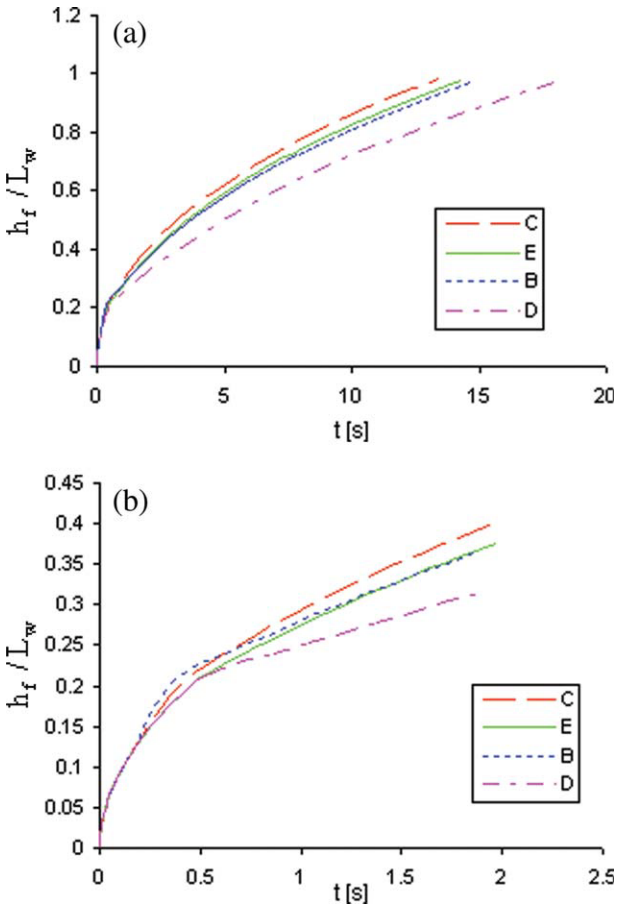

Figure 13. A comparison of evolution of the dimensionless and numerically predicted liquid-front height (h_f/L_w) in the wicks B, C, D, and E.

(a) The comparison till the time of full saturation. (b) The comparison in the first 2 s. [Color figure can be viewed in the online issue, which is available at wileyonlinelibrary.com.]

Table 3. Exact and Relative Time for Liquid Front to Reach Height of 0.07 m in Different Wicks

Wick	T7 (Time to Reach $h_f = 0.07$ m) (s)	{[T7(A) − T7]/T7 (A)} × 100 (%)
A	11.1471	0
B	13.091	−17.4
C	11.6152	−4.2
D	16.1555	−44.9
E	12.573	−12.8

right-most column of Table 3, which lists the relative wick-wetting time with respect to the wick A, alteration of wick geometry causes delay in reaching the wick end by the liquid front. All the altered wicks take more time to wet when compared with the simple wick. Note that the shortest and longest delays are in the wicks C and D, respectively.

As the absorption rate (or absorption speed) is inversely proportional to the measured times, so the right-most column is also indicative of the relative absorption rates in various wicks. It indicates that the wick alteration has reduced the absorption rate in general and this reduction is related to the length and diameter of the altered regions. The wicks C and D with 4.2 and 44.9% increase in the wicking time have the smallest and the largest reduction in the absorption rate when compared with the simple wick A.

Summary and Conclusion

Although the Washburn equation–based approach to model wicking in porous substrates is well established, the approach is not accurate for modeling the 2D and 3D capillary pressure–driven imbibitional flows as it is based on the assumption of 1D flow through a bundle of aligned tubes. We model the imbibition of liquids into polymer wicks, where a sharp flow front is clearly visible during the wicking process, using the flow physics of single-phase flow in porous media for flow behind the front. A computer program called PORE-FLOW© based on the FE/CV algorithm for the Darcy's law–based single-phase flow is developed to model the 3D wicking flows in complex-shaped wicks. The predictions of the program are first validated against the experimental results as well as the Darcy's law and Washburn equation–based analytical solutions for the 1D imbition in a cylindrical wick—it is observed that the numerical predictions follow the experimental results and the analytical solutions very closely. Later, the code is validated against the experimental results pertaining to imbibition in a complex wick with two different diameters. While the numerical predictions follow once again the experimental results very closely, the analytical solutions based on the Darcy's law and Washburn equation and using the 1D flow assumption, fail to be accurate. The excellent validation of our numerical simulation for the 1D and 3D wicking situations not only highlight the power of the single-phase Darcy's law–based wicking model but also point to another advantage of this model (vis-à-vis the Richard's equation approach described in the Introduction) in terms of being able to measure the model parameters quite easily.

Later, the code is then used to study wicking in four different wick shapes obtained by shaving off portions of cylindrical wicks. It is observed that these changes in the wick shape can have a significant impact on the mass of liquid imbibed into the wick, and reducing the wick diameter at appropriate places can be an effective way of controlling the wicking rate.

Notation

English letters

$\mathbf{A}$ = coefficient matrix (Eqs. 29 and 30)
B = constant coefficient (Eqs. 16a,b)
C = constant coefficient (Eqs. 16a,b)
D = diameter (m)
$\mathbf{F}$ = coefficient matrix (Eqs. 29 and 30)
f = parameter related to each element (Eq. 30), also filling factor
g = acceleration due to gravity (m/s^2)
H = head (m)
h = coordinate system aligned with the wick centerline (Figures 2 and 3)
K = permeability (m^2)
m = absorbed liquid mass (kg)
N = element shape function (Eq. 27)
$\mathbf{n}$ = normal vector (Eqs. 26 and 30)
P = modified pressure (Eq. 3)
p = liquid pressure (Pa)
Q = flow rate (Eq. 17d)
R = radius (m)
s = surface area (m^2)
t = time (s)
u = liquid velocity in h direction (m/s)
V = volume (m^3)
$\mathbf{v}$ = velocity vector (m/s)
w = weight function (Eq. 26)
x = x-coordinate (Eq. 26)
y = y-coordinate (Eq. 26)

Greek letters

θ = contact angle (°)
γ = surface tension of the liquid (N/m)
μ = viscosity of the liquid [kg/(m s)]
ε = porosity of the wick
ρ = liquid density (kg/m^3)
ϕ = probability density function (Eq. 14)
∇ = gradient operator
Γ = surface area of a CV surrounding an FE node (Eq. 34)

Superscripts

e = related to an element
t_n = nth time step

Subscripts

0 = initial value
1 = corresponding to the first wick region (Figure 3)
2 = corresponding to the second wick region (Figure 3)
atm = atmosphere
b = bead
c = capillary
e = effective
f = liquid front
h = hydraulic
i = interface between the two regions (Figure 3), also initial (time) (Eqs. 20 and 21)
j = index related to element number
k = element number
L = loss
s = suction
w = wick

Literature Cited

1. Lucas R. Rate of capillary ascension of liquids. *Kollid Z.* 1918;23: 15–22.

2. Washburn EV. The dynamics of capillary flow. *Phys Rev*. 1921;17:273–283.
3. Sutera SP. The history of Poiseuille's law. *Ann Rev Fluid Mech*. 1993;25:1–19.
4. Szekely J, Neumann AW, Chuang YK. The rate of capillary penetration and the applicability of the Washburn equation. *J Colloid Interface Sci*. 1971;35:273–278.
5. Masoodi R, Pillai K M, Varanasi P. Role of Hydraulic and Capillary Radii in Improving the Effectiveness of Capillary Model in Wicking. ASME Summer Conference. Jacksonville FL, USA, August 10–14, 2008.
6. Chatterjee PK. *Absorbency*. Amsterdam/New York: Elsevier, 1985.
7. Kissa E. Wetting and wicking. *Textile Res J*. 1996;66:660–668.
8. Chatterjee PK, Gupta BS. *Absorbent Technology*. Amsterdam: Elsevier, 2002.
9. Pan N, Gibson P. *Thermal and Moisture Transport in Fibrous Materials*. Cambridge: Woodhead, 2006.
10. Jacob B. *Dynamics of Fluids in Porous Media*. New York: Elsevier Science, 1972.
11. Scheidegger AE. *The Physics of Flow Through Porous Media*. Toronto: University of Toronto, 1974.
12. Dullien FAL. *Porous Media: Fluid Transport and Pore Structure*. San Diego: Academic Press, 1992.
13. Masoodi R, Pillai K M, Varanasi P. Darcy's law based models for liquid absorption in polymer wicks. *J AIChE*. 2007;53:2769–2782.
14. Pillai KM, Advani SG. Wicking across a fiber-bank. *J Colloid Interface Sci*. 1996;183:100–110.
15. Lockington DA, Parlange JY, Lenkopane M. Capillary absorption in porous sheets and surfaces subjected to evaporation. *Transp Porous Med*. 2007;68:29–36.
16. Glass RJ. Wetting front instability in unsaturated porous media: a three-dimentional study in initially dry sand. *Transp Porous Med*. 1990;5:247–268.
17. Wang Q-J, Horton R, Fan J. An analytical solution for one-dimensional water infiltration and redistribution in unsaturated soil. *Pedosphere*. 2009;19:104–110.
18. Crank J. *The Mathematics of Diffusion*, 2nd ed. New York: Oxford University Press, 1979.
19. http://www4dev.uwm.edu/porous/.
20. Whitaker S. *The Method of Volume Averaging*. Dordrecht: Kluwer Academic Publishers, 1999.
21. Tan H, Pillai KM. *Processing composites for blast protection*. In: Uddin N. editor. *Blast Protection of Civil Infrastructures and Vehicles Using Composites*. Cambridge: Woodhead, 2010.
22. Tan H, Pillai KM. Finite element implementation of stress-jump and stress-continuity conditions at porous-medium, clear-fluid interface. *Comput Fluids*. 2009;38:1118–1131.
23. Amestoy PR, Duff IS. Excellent J-YL. Multifrontal parallel distributed symmetric and unsymmetric solvers. *Comput Methods Appl Mech Eng*. 2000;184:501–520.
24. Tan H, Pillai KM. Effect of fiber-mat anisotropy on 1D mold filling in LCM: a numerical investigation. *Polym Compos*. 2008;29:869–882.

Manuscript received Aug. 17, 2009, revision received Mar. 16, 2010, and final revision received Jun. 18, 2010.